Supersonic Flutter and Buckling Optimization of Tow Steered Composite Plates

Guimarães, Thiago A.M.; Giovani Pereira Castro, Saullo; Cesnik, Carlos E. S.; Rade, Domingos A.

DOI
10.2514/1.J057282

Publication date
2019

Document Version
Accepted author manuscript

Published in
AIAA Journal: devoted to aerospace research and development

Supersonic Flutter and Buckling Optimization of Tow-Steered Composite Plates

Thiago A. M. Guimarães *
University of Uberlândia, Uberlândia, MG, 38408-100

Saullo G. P. Castro†
Delft University of Technology, Delft, The Netherlands

Carlos E. S. Cesnik‡
University of Michigan, Ann Arbor, Michigan 48109-2140

Domingos A. Rade§
Technological Institute of Aeronautics, São José dos Campos, SP, 12228-900

The supersonic aeroelastic stability of tow steered carbon reinforced composite panels, in each layer of which the fibers follow curvilinear paths, is assessed. A structural model based on the Rayleigh-Ritz method, combined with the aerodynamic piston theory, is derived to represent the aeroelastic behavior of rectangular plates under different boundary conditions. In this model, the Classical Lamination Theory, considering symmetric stacking sequence and fiber trajectories described by Lagrange polynomials of different orders, is used. In addition, manufacturing constraints, which impose limitations to the feasible fiber trajectories, and the effect of in-plane loads, are also considered in the model. Using a multi-criteria Differential Evolution algorithm, numerical optimization is performed for a variety of scenarios, aiming at increasing the flutter and linear buckling stability margins of tow-steered plates, considering the geometrical parameters defining the fiber trajectories on the layers as design variables. Results obtained for the different optimization scenarios are compared, having a composite plate with unidirectional fibers as the baseline, aiming at evaluating the benefits achieved by the optimum tow-steered plates. Results enable to quantify the stability improvements by exploring fiber steering, which has been shown to be beneficial, even in situations where manufacturing constraints are accounted for.

I. Nomenclature

a = Plate length

*Assistant Professor, Department of Mechanical Engineering, Av. João Naves de Ávila 2121, AIAA Member .
†Assistant Professor, Department of Aerospace Engineering , Kluyverweg 1, 2629 HS Delft, The Netherlands
‡Professor of Aerospace Engineering, Department of Aerospace Engineering, 1320 Beal Avenue. Fellow AIAA
§Professor, Technological Institute of Aeronautics, Praça Mal. Eduardo Gomes 50, Vila das Acácias, AIAA member

b	=	Plate width
$\boldsymbol{D}$	=	Out of plane stiffness matrix, according to the Classical Laminate Theory
E_1, E_2	=	longitudinal and transverse Young's moduli of a composite lamina
G_{12}	=	In-plane shear modulus of a Composite lamina
$I_{(1...5)}$	=	Material invariants
$\boldsymbol{K_a}, \boldsymbol{K_G}$	=	Aerodynamic and geometric stiffness matrices
$\boldsymbol{M}, \boldsymbol{K}$	=	Plate mass and stiffness matrix
$\boldsymbol{q}$	=	Generalized coordinates
$\boldsymbol{Mp}$	=	Vectors of moments
r, s	=	numbers of terms used to approximate the transverse displacement field in x and y directions
t	=	Ply thickness
T	=	Plate kinetic energy
U	=	Potential energy
u, v, w	=	Local plate deflection components in x,y,z directions, respectively
$V_{(1...4)}, W_{(1...4)}$	=	composite lamination parameters
x, y, z	=	Cartesian coordinates
w_0	=	Plate mid-plane transverse displacement
W	=	Virtual work done by aerodynamic load
α	=	Buckling eigenvalue problem
ΔP	=	Aerodynamic pressure
$\boldsymbol{\epsilon}$	=	Strain vector
ζ	=	Modal damping ratio
θ_{ij}	=	Fiber angle defined at (i,j) control points
Θ	=	Local fiber angle relative to the x-direction
$\boldsymbol{\kappa}$	=	Vector of plate curvatures
λ^*	=	Dimensionless aerodynamic parameter
μ_{12}	=	In plane Poisson's coefficient of a composite lamina
ρ	=	Mass density
χ	=	Eigenvalue of associated to the aeroelastic-buckling problem
$\boldsymbol{\Psi}$	=	Matrix forme from Rayleigh-Ritz approximation functions
ω	=	Natural frequency

II. Introduction

The safe design of panels against aeroelastic instability is driven by the determination of critical aerodynamic conditions regarding Mach number and dynamic pressure [1]. Specifically in the design of rockets and supersonic aircraft, the aeroelastic stability of composite panels is recognized as being worth of investigation.

Dowell[2] presents a review of panel flutter, introducing the theoretical mathematical analysis and correlations with experiments. Yang [3] proposed a double curved thin shell finite element for the modeling of composite plates, curved panels, and composite cylindrical shells. Mei and coworkers [4] developed finite element models to evaluate nonlinear flutter of composite panels considering the von Kàrman large-deflection strain-displacement relations in the time domain. Those authors also evaluated the nonlinear behavior of composite panels for different configurations regarding aspect ratios, lamination angles and number of layers[5]. Afterwards, different approaches were developed to improve design and control instabilities, such as active control based on piezoelectric actuators [6], consideration of stiffeners base as structural elements [7] and the use of electro-rheological fluids as a semi-active approach [8]. Marques et al. [9] proposed the use of evolutionary optimization algorithms to optimize panels considering different flow directions, elastic foundations and boundary conditions.

The classic strategy of aeroelastic tailoring consists in stacking plies in different orientations for achieving aeroelastic benefits. This design approach has been employed in different projects, such as the flight demonstrator X-29, in which the problem divergence taking place at low speed was solved by arranging the stacking sequence to explore the bending-torsion coupling in its composite wings [10].

More recently, the emergence and development of automated manufacturing procedures culminated with the development of novel, more efficient designs of composite laminates. The automated fiber placement (AFP) process currently enables to manufacture the so-called *variable stiffness composite laminates* (VSCL), understood as those whose local membrane and bending stiffnesses vary spatially over the laminate. This goal can be attained by varying the fiber/matrix volume ratio or by varying the fiber trajectories. This last case characterizes the tow-steered composites which are studied in this paper.

A number of previous research studies have demonstrated the possibility of achieving improved behavior of VSCL as compared to traditional laminates, under different design goals. A number of studies have been reported in the literature, in which VSCL could be designed to improve buckling resistance [11], reduce stress concentrations around holes [12], maximize the fundamental natural frequency [13], and optimize aeroelastic characteristics of a composite wing structure [14–17]. The work of Fazilati [18] presents the effect of delamination in the panel flutter behavior. However, some practical limitations must still be addressed.

The impact of manufacturing defects in VSL, especially the effects of gaps and overlaps, had not been addressed in the literature until recently [19] . The “defect layer" method highlights the influence of defects on the critical buckling load and in-plane stiffness [20].

The most common approach to design and manufacture variable stiffness plates consists in defining the steering angle as functions of its values on the edges of the plate, which provides easy control of the turning radius from these parameters. It has been verified that the occurrence of defects depends mainly on the turning radius, whose minimum value is determined by the fiber tape width[21].

As compared to traditional non-steered counterparts, the difficulty in optimizing tow-steered laminates is a consequence of the larger number of design variables required to define the fiber trajectory, layer thicknesses and manufacturing constraints [22].

In this context, this paper proposes an improved numerical strategy for buckling and aeroelastic tailoring of tow-steered composite panels under supersonic flow, considering manufacturing constraints. The problem is tackled in a multi-criterion optimization framework, in which the critical buckling load and the flutter speed are chosen as objective functions, and the parameters defining the fiber trajectories are the design variables.

The paper is organized as follows:under the hypotheses of linear elasticity and Classical Lamination Theory (CLT), a symmetric low-dimension structural laminate model is derived based on the Rayleigh-Ritz (Assumed-Modes) approach. The modeling procedure is duly adapted to accommodate curvilinear fiber trajectories, which are represented by Lagrange polynomials whose orders can be arbitrarily chosen. The structural model is associated to the supersonic Piston Theory to account for aerodynamic loads. First, the accuracy of structural model is verified by comparing a set of natural frequencies and corresponding vibration mode shapes with their counterparts obtained from finite element analyses. Then, the flutter and buckling instability boundaries are simultaneously optimized in a multi-objective optimization framework. Numerical optimization is performed for simply-supported, constant thickness plates, considering different orders of the polynomials used to interpolate the fiber trajectories. These orders determine the numbers of design variables. A Differential Evolution (DE) algorithm is used to solve the constrained optimization problems. In recognition of the importance of minimizing manufacturing defects, the optimization problem is reformulated in order to account for the limitations imposed to the fiber trajectories.

III. Formulation

Figure 1(a) depicts the i-th ply of a rectangular tow-steered laminate of dimensions $a \times b$, positioned on the xy plane, in which $\theta(x, y)$ denotes the local fiber angle (steering angle) defined with respect to the ply axis x. Also indicated are the laminate global axes XY, with respect to which the ply is oriented according to the angle Φ_i.

In Fig. 1(b) a single fiber is illustrated, as well as a set of points of coordinates (x_m,y_n), named herein *control points*, which are used to define the function $\theta(x, y)$.

It is important to mention that once the fiber trajectories are defined for each ply according to $\theta(x, y)$, the laminate is obtained by stacking plies with different orientations with respect to the global axes, according to the angles $\Phi_i, i = 1, 2...$, in a procedure similar to that employed in traditional composite laminates.

In the formulation that follows, the local fiber angle is represented as a function of the lamina coordinates x,y and the angle values at the control points θ_{mn} in terms of Lagrange polynomials, following the approach proposed by Wu et al. [22], as follows:

$$\theta_i(x,y) = \Phi_i + \sum_{m=0}^{M}\sum_{n=0}^{N}\theta_{mn}\prod_{k=0,k\neq m}^{M}\frac{x-x_k}{x_m-x_k}\cdot\prod_{p=0,p\neq n}^{N}\frac{y-y_p}{y_n-y_p}. \tag{1}$$

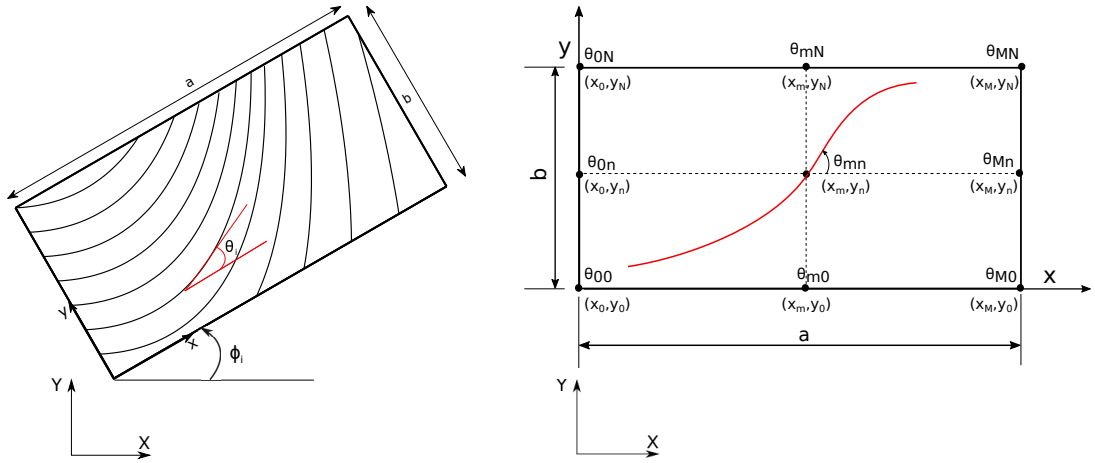

Fig. 1 Illustration of an individual ply of a tow-steered composite laminate. (a) indication of steering and ply orientation angles; (b) indication of control points used to interpolate the steering angle.

It should be mentioned that, as the order of the polynomial increases, the nonlinearity of the fiber trajectories also increases, and larger numbers of alternative fiber paths can be obtained.

The laminate is modeled by assuming that each ply is under plane stress state and small strains; linear material behavior is assumed. Under the assumptions of CLT, and considering only symmetric laminates (to avoid membrane-bending coupling), the following relation between moments and curvature is obtained:

$$\boldsymbol{M}_p\,(x,y) = \boldsymbol{D}\,(x,y)\,\boldsymbol{\kappa}\,(x,y), \tag{2}$$

in which, $\boldsymbol{M}_p\,(x,y)$ is the vector of moments, $\boldsymbol{\kappa}\,(x,y)$ is the vector of curvatures, and $\boldsymbol{D}\,(x,y)$ is the stiffness matrix. In the case of tow-steered, this matrix must be computed accounting for the fiber angle variation over the ply according to Eq. 1, as proposed by Wu et al.

Matrix $\boldsymbol{D}$, derived from a combination of lamination parameters (W_i) (i=1 to 4), and invariants I_i (i=1 to 5), is

expressed as follows:

$$\begin{bmatrix} D_{11}(x,y) & D_{12}(x,y) & D_{16}(x,y) \\ D_{12}(x,y) & D_{22}(x,y) & D_{26}(x,y) \\ D_{16}(x,y) & D_{26}(x,y) & D_{66}(x,y) \end{bmatrix} = \frac{h^3}{12}\left[\mathbf{\Gamma_0} + \mathbf{\Gamma_1} W_1(x,y) + \mathbf{\Gamma_2} W_2(x,y) + \mathbf{\Gamma_3} W_3(x,y) + \mathbf{\Gamma_4} W_4(x,y)\right], \quad (3)$$

where h is the total thickness of the laminate.

The expressions for the laminate invariants gathered in matrices $\mathbf{\Gamma_0}$ to $\mathbf{\Gamma_4}$ are omitted here and can be found in references [23, 24].

In Equation 3 it can be seen that the components of the stiffness matrix are functions of coordinates x and y, which implies that the local stiffness depends on the position over the plate, and justifies the denomination "variable stiffness composites" given to tow-steered composite laminates.

Accounting for the effects of in-plane normal and shear loads (N_{xx}, N_{yy}, N_{xy} [N/m]), based on the hypotheses of the Kirchhoff's plate theory, which is adequate for thin plates, the total potential and kinetic energies of the plate are given, respectively, as [25]:

$$U = \frac{1}{2}\int_0^a \int_0^b \kappa^T \mathbf{D} \kappa dx dy - \frac{1}{2}\int_0^a \int_0^b \left[N_{xx}\left(\frac{\partial w}{\partial x}\right)^2 + N_{yy}\left(\frac{\partial w}{\partial y}\right)^2 + 2N_{xy}\frac{\partial w}{\partial x}\frac{\partial w}{\partial y}\right] dxdy, \quad (4)$$

$$T = \frac{1}{2}\rho h \int_0^b \int_0^a \left(\frac{\partial w}{\partial t}\right)^2 dxdy, \quad (5)$$

where ρ is the material density.

In the context of the Rayleigh-Ritz approach, the transverse displacement field for a fully simply-supported plate is approximated as:

$$w(x,y,t) = \sum_{r=r_0}^{r_{max}} \sum_{s=s_0}^{s_{max}} q_{rs}(t) sin\left(r\frac{x}{a}\right) sin\left(s\frac{y}{b}\right) = \mathbf{\Psi q}, \quad (6)$$

where $\mathbf{\Psi}$ is the $1 \times (r_{max} - r_0 + 1)(s_{max} - s_0 + 1)$ matrix formed by the approximation functions and $\mathbf{q}$ is the $(r_{max} - r_0 + 1)(s_{max} - s_0 + 1) \times 1$ vector of generalized coordinates.

The flow is assumed to occur in direction X. Aerodynamic loads are modeled based on potential flow assumptions. The aerodynamic pressure ΔP, modeled according to the method proposed by Ashley [1], known as first order Piston Theory, with dissipative effects neglected [26], is expressed as follows:

$$\Delta P = \lambda \frac{\partial w}{\partial x}, \quad (7)$$

λ being the parameter that represents the airflow conditions, defined as:

$$\lambda = \frac{\rho_\infty U_\infty^2}{\sqrt{M_\infty^2 - 1}}, \tag{8}$$

where M_∞ is the Mach number, U_∞ is the flow velocity and ρ_∞ is the air density.

The aeroelastic model is obtained by combining the expressions of the potential energy (Eq. 4), kinetic energy (Eq 5), aerodynamic generalized forces, and the Lagrange's equations [25]. Such a procedure leads to the following set of coupled, second order, differential equations:

$$\mathbf{M}\ddot{\mathbf{q}}(t) + (\lambda \mathbf{K_a} + \alpha \mathbf{K_G} + \mathbf{K})\,\mathbf{q}(t) = \mathbf{0}, \tag{9}$$

where $\mathbf{M}$ is the mass matrix, $\mathbf{K_a}$ is the aerodynamic stiffness matrix, $\mathbf{K_G}$ is the geometric stiffness matrix, and $\mathbf{K}$ is the structural stiffness matrix. In addition, α is the membrane load parameter.

Searching for the solution of Eq. 9 under the form $\mathbf{q}(t) = \overline{\mathbf{q}} e^{\chi t}$, the following eigenvalue problem is obtained, which must be used for the combined linear buckling and aeroelastic stability analyses:

$$\left(\lambda \mathbf{K_a} + \alpha \mathbf{K_G} + \mathbf{K} + \chi^2 \mathbf{M}\right) \overline{\mathbf{q}} = \mathbf{0}. \tag{10}$$

IV. Model validation

In this section, the Rayleigh-Ritz-based structural model (referred to as RR) described above is verified and validated by comparing a set of natural frequencies and buckling loads obtained from the resolution of Eq. 10, disregarding the aerodynamic term, with the counterparts obtained from finite element discretization using the commercial software NASTRAN, for both unidirectional and tow steered configurations. It should be mentioned that such a validation is indispensable since the predictive capability of Rayleigh-Ritz models strongly depends on the type and number of approximation functions used in Eq. 6. However, the aeroelastic behavior is not included in this validation.

The FE model construted consists of 4800 rectangular CQUAD4 shell elements (80 elements in the spanwise direction and 60 elements in the chordwise direction). Mesh convergence was checked to guarantee adequate convergence of the first six natural frequencies.

For the computation of the natural frequencies of the tow-steered configuration using NASTRAN, a methodology was developed to take into consideration arbitrary fiber paths by ascribing different fiber orientations to standard unidirectional fiber elements, according to their positions over the plate. Such a procedure is described in [17] .

Table 1 shows the material properties of an individual lamina chosen for the numerical simulations of the panels considered in this section. Simply-supported boundary conditions are assumed for all the edges of the plate.

Table 1 Lamina physical properties and dimensions

Property	Value	Property	Value
E_1	129500 MPa	a	400 mm
E_2	9370 MPa	b	300 mm
G_{12}	5240 MPa	ρ	1500 kg/m^3
μ_{12}	0.38	Ply thickness, t	0.19 mm

Model validation is performed for two different plate configurations. Configuration **A** is a traditional unidirectional laminate, while configuration **B** is tow-steered. For configuration **A**, the stacking sequence of the eight layers has been defined as $[0^o/45^o/-45^o/90^o]_s$, and the material properties are given in Table 1. For configuration **B**, the fiber deposition course, which is illustrated in Fig. 3 for both RR and NASTRAN models, is defined according to Eq. 1, using second order Lagrange polynomials. It should be noticed that the stacking sequence defined for configuration **A** is also used for configuration **B**, by setting accordingly the values of the angles Φ_i appearing in Eq. 1.

The accuracy of the first six natural frequencies computed can be evaluated in Table 2 for configuration **A**, and in Table 3 for configuration **B**. In addition, Figure 2 portrays in color scale the values of the modal assurance criterion (MAC), used to evaluate the degree of collinearity between natural mode shapes obtained from RR and NASTRAN.

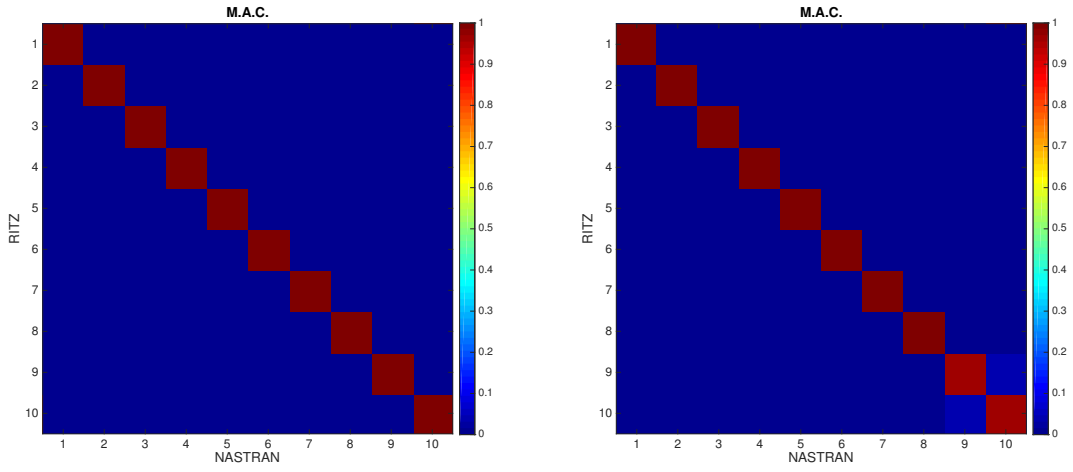

Fig. 2 Mode Assurance Criteria for: (a) configuration A; (b) configuration B

It can be seen that: i) for both configurations, the RR models provide satisfactory accuracy as compared to FE counterparts. The discrepancies between the values of the natural frequencies, though small for all the numbers of approximation functions considered, diminish monotonically as these numbers are progressively increased. One considers $r_{max} = 6$, $s_{max} = 6$ sufficient to guarantee the model convergence with an acceptable error of 0.65% for the steered configuration; ii) fiber steering exerts noticeable influence on the values of the natural frequencies; the intensity of such an influence varies from one mode to the other. Based on this later observation, the possibility of maximizing

the fundamental natural frequency by optimization of the steering path was addressed in references [27, 28] .

Table 2 **Values of natural frequencies obtained by Rayleigh-Ritz and the FE models for configuration A**

	ω_1 (Hz)	ω_2 (Hz)	ω_3 (Hz)	ω_4 (Hz)	ω_5 (Hz)	ω_6 (Hz)
Nastran	**64.16**	**153.44**	**168.12**	**252.48**	**312.5**	**335.40**
r_{max}=3, s_{max}=3	64.64	154.26	169.10	254.81	315.60	337.37
	(0.57)	(0.49)	(0.48)	(0.85)	(0.44)	(0.37)
r_{max}=4, s_{max}=4	64.53	154.20	168.93	254.63	313.88	336.64
	(0.56)	(0.40)	(0.45)	(0.68)	(0.41)	(0.36)
r_{max}=5, s_{max}=5	64.52	154.06	168.88	254.20	313.80	336.62
	(0.50)	(0.39)	(0.40)	(0.66)	(0.35)	(0.33)
r_{max}=6, s_{max}=6	64.48	154.05	168.81	254.16	313.62	336.51
	(0.50)	(0.35)	(0.39)	(0.60)	(0.34)	(0.32)
r_{max}=7, s_{max}=7	64.48	153.99	168.79	254.00	313.59	336.50
	(0.45)	(0.35)	(0.37)	(0.59)	(0.32)	(0.31)
r_{max}=8, s_{max}=8	64.45	153.98	168.76	253.98	313.52	336.45
	(0.45)	(0.33)	(0.37)	(0.56)	(0.31)	(0.31)

* Values indicated between parentheses are percent deviations

Table 3 **Values of natural frequencies obtained by Rayleigh-Ritz and the FE models for configuration B**

	ω_1 (Hz)	ω_2 (Hz)	ω_3 (Hz)	ω_4 (Hz)	ω_5 (Hz)	ω_6 (Hz)
Nastran	**65.67**	**152.39**	**171.75**	**250.43**	**322.20**	**333.53**
r_{max}=3, s_{max}=3	66.03	153.29	172.80	252.79	326.56	337.03
	(0.54)	(0.59)	(0.60)	(0.94)	(1.35)	(1.04)
r_{max}=4, s_{max}=4	66.00	153.03	172.49	252.26	324.34	335.19
	(0.50)	(0.42)	(0.42)	(0.72)	(0.66)	(0.49)
r_{max}=5, s_{max}=5	66.00	153.01	172.47	252.11	323.34	334.79
	(0.50)	(0.40)	(0.41)	(0.66)	(0.35)	(0.37)
r_{max}=6, s_{max}=6	65.97	152.98	172.43	252.08	323.31	334.69
	(0.45)	(0.38)	(0.39)	(0.65)	(0.34)	(0.34)
r_{max}=7, s_{max}=7	65.97	152.95	172.41	251.96	323.30	334.68
	(0.45)	(0.36)	(0.38)	(0.60)	(0.33)	(0.34)
r_{max}=8, s_{max}=8	65.96	152.94	172.39	251.94	323.25	334.64
	(0.44)	(0.36)	(0.37)	(0.60)	(0.32)	(0.32)

* Values indicated between parentheses are percent deviations

Additionally, the verification of the accuracy of buckling loads are shown in Table 4, for configurations **A** and **B**, assuming only membrane loads N_{xx} applied to the plate. Again, $r_{max} = 6$, $s_{max} = 6$ were sufficient to guarantee the satisfactory maximum error of 0.9% for both configurations considered.

Table 4 Values of buckling loads obtained by Rayleigh-Ritz and the FE models

	Buck Load CA N_{xx} (N/m)	Buck Load CB N_{xx} (N/m)
Nastran	5986	6263
r_{max}=3, s_{max}=3	6077 (1.5)	6330 (1.1)
r_{max}=4, s_{max}=4	6053 (1.1)	6323 (1.0)
r_{max}=5, s_{max}=5	6053 (1.1)	6323 (1.0)
r_{max}=6, s_{max}=6	6043 (0.9)	6317 (0.85)
r_{max}=7, s_{max}=7	6043 (0.9)	6317 (0.85)
r_{max}=8, s_{max}=8	6040 (0.9)	6313 (0.8)

* Values indicated between parentheses are percent deviations

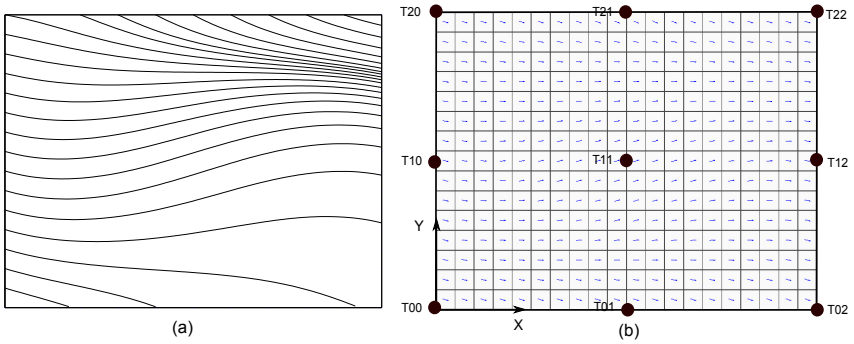

Fig. 3 Steered lamina: (a) Rayleigh-Ritz model; (b) FE Model

V. Optimization procedure

In spite of typically high computation cost, evolutionary algorithms have been proven to be effective in solving complex optimization problems, since they enable a more effective search over the solution space, thus increasing the probability of reaching the global minimum. In addition, those algorithms do not require the computation of gradients, thus being well adapted to deal with discontinuous objective functions and mixed continuous-discrete design variables [29, 30]. Based on the previous experience of the authors with the use of Differential Evolution (DE) algorithm [17] was used to obtain the maximum buckling/aeroelastic stability margin of non-steered and steered eight layer plates, based on the model described by Eq. 9. In addition, the optimization tests were carried-out considering suitable numbers of individuals in the populations (at least 6 times the number of design variables) and generations of the DE algorithm. Given the stochastic nature of the optimization method, five runs were performed for each optimization test.

Five different optimization scenarios have been defined, as illustrated in Fig. 4: the first (**O1**) considers non-steered fiber trajectories and admissible discrete fiber angles (90^o, $+45^o$, 0^o, -45^o). The second (**O2**) considers also a non-steered plate, but the fiber angle of each of the eight layers can vary continuously from -90^o to $+90^o$. In the third optimization (**O3**), one considers a tow steered plate with fiber paths defined by first order Lagrange polynomials in both x and y

directions. Similarly, in the fourth (**O4**) and fifth optimizations (**O5**), the fiber trajectories are defined by second order and third order Lagrange polynomials, respectively. In all cases, the layups are kept symmetric. For optimizations (**O3**), (**O4**) and (**O5**), the layup adopted for (**O1**) is also used.

As can be seen in Fig. 4, for the optimizations involving tow-steered plates, the number of design variables, which are the control angles, increases from 4 to 16 as the order of the polynomials used to represent the fiber paths is increased from 1 to 3.

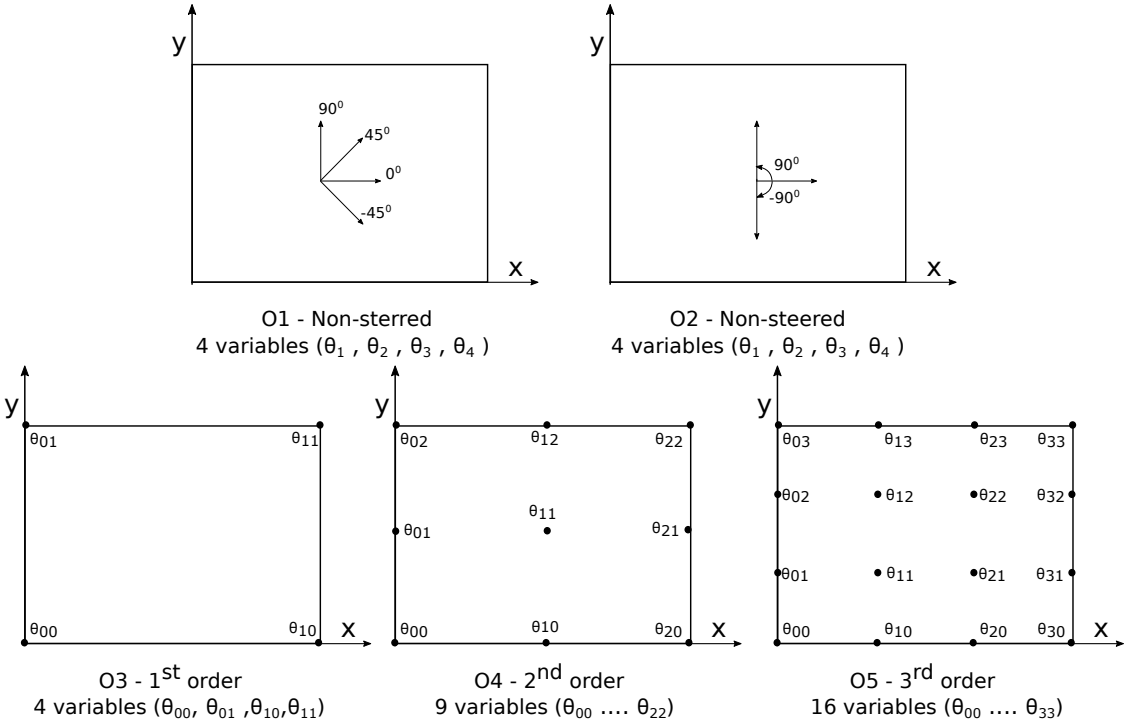

Fig. 4 Configurations adopted for optimization

In Table 5 are summarized the descriptions of each optimization, the respective design variables and their types, as well as the lateral constraints imposed to the design variables. Therefore, the optimization problem can be stated as:

$$\textit{Maximize: } \mathcal{J}_1(\theta_i) = \lambda^*_{flutter},$$

Design Variables: as per second column of Table 5,

subject to: as per fourth column of Table 5

A. Augmented design space

Besides the optimization scenarios defined above, two additional scenarios, characterized by broader design spaces, have been considered, as described in Tab. 6. The proposed configurations, denoted by **O3-a** and **O4-a** are similar to

Table 5 Characteristics of the five optimization scenarios defined

Configuration	Design Variables	Variables Types	Boundaries
O1	$[\theta_1 \quad \theta_2 \quad \theta_3 \quad \theta_4]$	Discrete	$[\pm 45^o \quad 0^o \quad 90^o]$
O2	$[\theta_1 \quad \theta_2 \quad \theta_3 \quad \theta_4]$	Continuous	$[-90^o \quad 90^o]$
O3	$\begin{bmatrix} \theta_{01} & \theta_{11} \\ \theta_{00} & \theta_{10} \end{bmatrix}$	Continuous	$[-90^o \quad 90^o]$
O4	$\begin{bmatrix} \theta_{02} & \theta_{12} & \theta_{22} \\ \theta_{01} & \theta_{11} & \theta_{21} \\ \theta_{00} & \theta_{10} & \theta_{20} \end{bmatrix}$	Continuous	$[-90^o \quad 90^o]$
O5	$\begin{bmatrix} \theta_{03} & \theta_{13} & \theta_{23} & \theta_{33} \\ \theta_{02} & \theta_{12} & \theta_{22} & \theta_{32} \\ \theta_{01} & \theta_{11} & \theta_{21} & \theta_{31} \\ \theta_{00} & \theta_{10} & \theta_{20} & \theta_{30} \end{bmatrix}$	Continuous	$[-90^o \quad 90^o]$

configurations **O3** and **O4**, respectively, but the possibility of having different fiber paths among the layers is considered, thus resulting in increased numbers of design variables: from 4 for **O3** to 16 for **O3-a**, and from 9 for **O4** to 36 for **O4-a**. In these cases Eq. 1 is slight changed for:

$$\theta_i(x,y) = \sum_{m=0}^{M}\sum_{n=0}^{N}\theta_{mni}\prod_{k=0,k\neq m}^{M}\frac{x-x_k}{x_m-x_k}\cdot\prod_{p=0,p\neq n}^{N}\frac{y-y_p}{y_n-y_p} \tag{11}$$

Table 6 Lay-up options and design variables for the increased desing space

Configuration	Design Variables	N. of Variables	Boundaries
O3-a	$\begin{bmatrix} \theta_{01i} & \theta_{11i} \\ \theta_{00i} & \theta_{10i} \end{bmatrix} i(1...4)$	16	$[-90^0 \quad 90^0]$
O4-a	$\begin{bmatrix} \theta_{02i} & \theta_{12i} & \theta_{22i} \\ \theta_{01i} & \theta_{11i} & \theta_{21i} \\ \theta_{00i} & \theta_{10i} & \theta_{20i} \end{bmatrix} i(1...4)$	36	$[-90^0 \quad 90^0]$

B. Manufacturing Constraints

As mentioned before, there is usually a direct relation between the increase of polynomial order and the complexity of the optimized fiber trajectory. Complex, large-curvature paths can be unfeasible in practice due to limitations of the AFP machines. In the current stage of manufacturing technology, the realization of tow-steered composites is limited due to the fact that fiber trajectories with small curvature radius are frequently associated to larger densities of defects (gaps and overlaps). In this sense, a convenient strategy proposed in the literature to tackle this limitation consists in introducing manufacturing constraints, in which the the fibers are placed following constant curvature courses [20]. Hence, programming of the AFP machine becomes easier and the density of defects can be controlled in terms of the

turning radius.

To comply with manufacturing limitations, the tow steered fiber path over an individual ply is formulated in terms of three parameters (Φ_i, θ_0 and θ_1), where θ_0 and θ_1 are, respectively, the fiber angles at $x = 0$ and $x = a$. Accordingly, the turning radius is determined in terms of these parameters as follows [31]:

$$r = \frac{a}{sin\theta_1 - sin\theta_0}. \tag{12}$$

It should be mentioned that the turning radius is the most relevant manufacturing parameter that should be taken into account to avoid local buckling, out-of-plane fiber wrinkle and crimping, which are prone to degrade the mechanical properties of the laminate. Therefore, considering a typical tow width (3.17mm) the minimum turning radius allowable is found to be 635mm; this value will be used to constrain the fiber paths.

Under these conditions, the steering angle, considering constant turning radius, is expressed as:

$$sin\theta(x) = sin\theta_0 + (sin\theta_1 - sin\theta_0)\frac{x}{a}, \tag{13}$$

and the fiber trajectory, obtained by integration of $dy/dx = \tan\theta$, is found to be expressed as:

$$y(x) = \frac{a\sqrt{1 - \left(\sin\theta_0 - \frac{x\,(\sin\theta_0 - \sin\theta_1)}{a}\right)^2}}{\sin\theta_0 - \sin\theta_1} \tag{14}$$

Hence, it can be seen that parameters θ_0, θ_1 and a fully define the fiber path with constant curvature and allows the inclusion of manufacturing constraints. This approach is slight different from the work of C. Walmart et al [32], in which was considered the fiber placement in parallel.

VI. Optimization Results

The results of two groups of optimization tests are presented next: the first group is related to optimizations **O1** to textbfO5, defined in Table 4, for which no manufacturing constraints are considered and in-plane loads are disregarded (which means that matrix $\mathbf{K_G}$ is not considered in Eq. 9). In the second group, the optimization problem is reformulated to account for in plane-loads and manufacturing constraints, as expressed by Eq. 14, and considers multi-criterion optimization of buckling and flutter behavior.

A. Mono-criterion flutter optimization

Table 7 summarizes the optimization results, including the critical values of the dimensionless aerodynamic parameter $\lambda^* = \lambda a^3/(G_{12}h^3)$, while Fig. 5 illustrates the fiber trajectories obtained for the tow steered configurations

O3, **O4** and **O5**. Although not shown here, the onset of aeroelastic instability is determined from successive analyses of the eigenvalues of Eq. 10 for increasing values of the aerodynamic parameter λ, being characterized by the coalescence of two natural frequencies and the occurrence of negative damping factors.

Table 7 Optimization Results

Configuration	Optimal Values	Flutter [λ^*]	Improvement *
O1	$[0° \quad 0° \quad 0° \quad 45°]$	779	—
O2	$[-24.24° \quad 31.79° \quad 31.67° \quad 24.95°]$	812	4.47%
O3	$\begin{bmatrix} 64.98° & -64.56° \\ -15.23° & 11.34° \end{bmatrix}$	796	2.46%
O4	$\begin{bmatrix} -77.57° & -26.31° & -83.35° \\ 50.71° & 7.88° & 53.40° \\ -74.33° & -34.21° & -63.44° \end{bmatrix}$	866	11.41%
O5	$\begin{bmatrix} 39.95° & -75.60° & -69.75° & -14.01° \\ -32.67° & -10.82° & 8.23° & 30.14° \\ -49.58° & 11.18° & -11.42° & 55.71° \\ -15.15° & -55.95° & 60.09° & 1.65° \end{bmatrix}$	937	20.50%

* Improvements of flutter speed with respect to optimization O1.

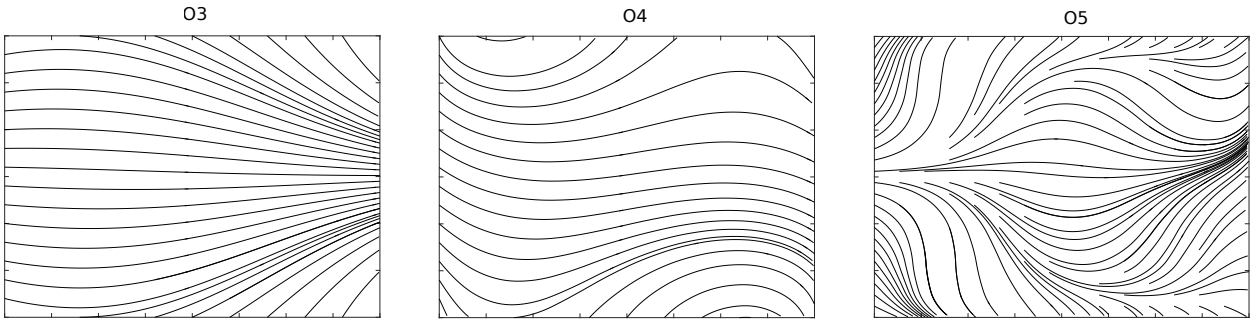

Fig. 5 Optimized trajectories for configurations O3, O4 e O5

Taking the optimized configuration obtained for **O1** as reference, it can be noticed that the optimized configurations obtained for **O2** , **O3** , **O4** and **O5** provide indeed increased flutter speeds, which means improved aeroelastic stability margins. In addition, for the tow-steered configurations, the degree of improvement increases with the order of the polynomials used to described the fiber trajectories. This is expected since higher polynomial orders correspond to higher numbers of design variables (thus broader design spaces). Nonetheless, it can be seen that as the order of the polynomials increases, more complex fiber paths are obtained, which, in practical cases, can be infeasible due to manufacturing constraints.

As mentioned before, 5 runs were performed for each optimization case. Figure 6 illustrates the evolution of the DE optimization for each of those runs, for cases **O2** , **O3** , **O4** and **O5**.

Even though the results above were obtained disregarding in-plane loads, it was found interesting to check the

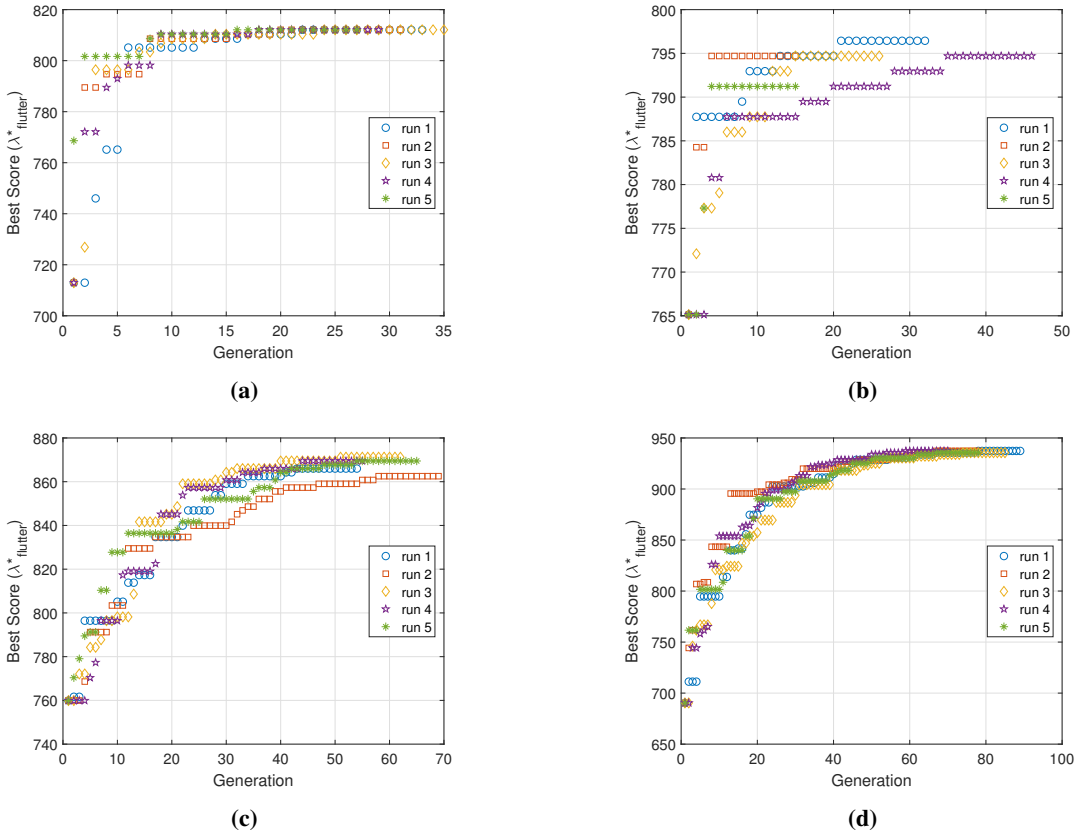

Fig. 6 Evolution of the DE optimization runs. (a) O2; (b) O3; (c) O4; (c) O5

combined flutter-buckling behavior of the five optimized plates, according to Eq. 10, assuming the presence of the N_{xx} membrane load. The results are shown in Fig. 7, in which the stability zone comprises the leftmost region of the graph. It can be seen that the steered configurations **O3**, **O4** and **O5** have quite similar buckling behaviors. In addition, the non-steered configuration **O2**, optimized with continuous angles, presents the best results regarding buckling.

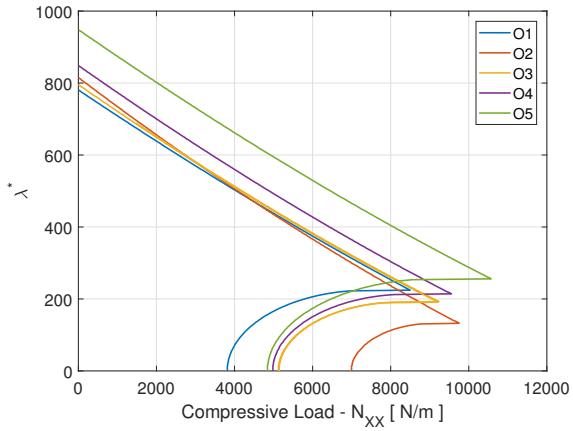

Fig. 7 Combined buckling-flutter evaluation

The results for optimizations **O3-a** and **O4-a** are given in Tab. 8, indicating better performance when compared to counterparts **O3** and **O4**. This can be explained by the larger numbers of design variables, since the fiber fiber trajectories on each layer were considered independently from the others. Certainly, this is an interesting result since manufacturing of configurations **O3-a** and **O4-a** would only imply minor increase in the complexity of AFP machine programming.

Similarly to Fig. 6, 8 illustrates the evolution of the 5 optimization runs, for both **O3-a** and **O4-a**. It is apparent from these late that the differences of the convergence features from one run to the others, are more significant for **O4-a** than for **O3-a**. Again, this behavior can be explained by the much larger number of design variables involved in **O4-a**.

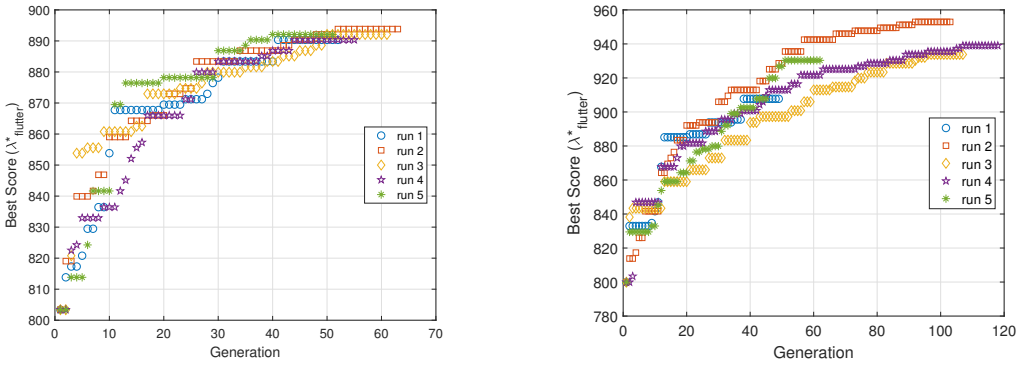

Fig. 8 Evolution of the DE optimization runs. (a) O3-a; (b) O4-a

B. Flutter-buckling multi criteria optimization

The results shown in Fig. 7 lead to conclude that the requirements for flutter and buckling stability can be conflicting with each other. Therefore, the possibility of increasing the combined flutter-buckling stability margin in the λ^*-α plane for tow-steered plates following a multi-objective optimization approach was investigated, being considered in this sub-section.

The multi-objective optimization problem is stated as:

$$
\begin{aligned}
\textit{Maximize: } & \mathcal{J}_1(\theta_i) = \lambda^*(\theta_i), \\
& \mathcal{J}_2(\theta_i) = \text{buckling load}(\theta_i), \\
\textit{subject to: } & -90^\circ \leq \theta_i \leq 90^\circ \\
& \text{under constraints as per fourth column of Table 9;}
\end{aligned}
$$

Four other configurations were evaluated, as detailed in Table 9. Configuration **O6** keeps the stacking sequence adopted in **O1**, adopts constant curvature fiber placement, and accounts for the manufacturing constraints ($r > 635mm$)

Table 8 Optimization Results for the augmented design space

Configuration	Optimal Values	Flutter [λ^*]	Improvement *
O3-a	$\begin{bmatrix} -44.62° & 48.01° \\ -44.49° & 25.41° \end{bmatrix}$ $i = 1$ $\begin{bmatrix} 61.95° & -56.38° \\ 45.70° & -41.92° \end{bmatrix}$ $i = 2$ $\begin{bmatrix} 58.08° & -62.17° \\ 36.27° & -51.28° \end{bmatrix}$ $i = 3$ $\begin{bmatrix} 10.09° & -0.22° \\ 76.93° & -24.38° \end{bmatrix}$ $i = 4$	892	14.5%
O4-a	$\begin{bmatrix} -39.31° & -51.59° & -72.46° \\ 57.98° & 29.08° & 59.34° \\ -67.24° & -51.59° & -54.54° \end{bmatrix}$ $i = 1$ $\begin{bmatrix} 66.84° & 30.80° & -52.42° \\ -53.38° & -33.36° & -49.75° \\ -68.22° & 45.15° & -2.41° \end{bmatrix}$ $i = 2$ $\begin{bmatrix} -40.32° & 35.13° & -30.60° \\ -56.56° & -29.13° & -61.69° \\ -33.46° & 21.62° & 85.40° \end{bmatrix}$ $i = 3$ $\begin{bmatrix} -3.37° & -11.28° & 60.49° \\ 30.26° & -16.26° & -26.40° \\ 51.39° & 38.64° & -40.36° \end{bmatrix}$ $i = 4$	952	22.2%

* Improvements of flutter speed with respect to optimization O1.

according to subsection V-B; configuration **O7** is similar to configuration **O4** without any constraint imposed. Configurations **O8** and **O9** explore the augmented design space (Section V-A), being **O8** similar to **O6**, with the fiber paths on each ply optimized separately, and considering constant curvature and manufacturing constraints; finally, configuration **O9** is similar to configuration **O3-a** considering the optimization of the fiber paths of each ply separately, disregarding manufacturing constraints

Optimization computations were performed using a multi-criteria version of Differential Evolution algorithm [30] . The optimal solutions (Pareto fronts) for configurations **O6**, **O7**, **O8** and **O9** are shown in Fig. 9. It can be seen that configuration **O6** exhibits a much inferior performance as compared to the other configurations, which is expected since this configuration explores a reduced design space considering the same fiber path for all plies, under manufacturing constraint. The optimization solution **O7** provides the trade-off in a range of flutter onset ($\lambda^*_{flutter}$) from 730 and to 855 and buckling resistance from 5000 N/m to 6750 N/m. Moreover, configuration **O8** exhibits much superior performance, mainly regarding buckling load, as compared to configuration **O6**. This is expected since **O8** explores a broader design

Table 9 Configurations and design variables used in multi-objective flutter-buckling optimization

Configuration	Design Variables	Boundaries	Constraint
O6	θ_0, θ_1	$[-90^0 \quad 90^0]$	$r > 635mm$
O7	$\begin{bmatrix} \theta_{02} & \theta_{12} & \theta_{22} \\ \theta_{01} & \theta_{11} & \theta_{21} \\ \theta_{00} & \theta_{10} & \theta_{20} \end{bmatrix}$	$[-90^0 \quad 90^0]$	–
O8	θ_{0i}, θ_{1i} $i(1...4)$	$[-90^0 \quad 90^0]$	$r > 635mm$
O9	$\begin{bmatrix} \theta_{01i} & \theta_{11i} \\ \theta_{00i} & \theta_{10i} \end{bmatrix}$ $i(1...4)$	$[-90^0 \quad 90^0]$	–

space. The last optimization **O9** produces the best results regarding the flutter behavior in a range of buckling load from 6750 N/m to 7150 N/m.

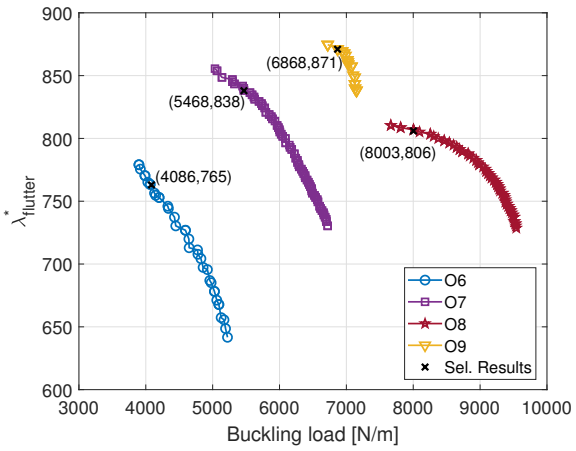

Fig. 9 Pareto fronts obtained from multi-criteria optimization runs for configurations O6, O7, O8 and O9.

The stability diagrams for the optimal solutions indicated in Fig. 9 with black stars are depicted in Fig. 10. It can be seen that constant-radius tow-steering does not provide any significant stability improvement considering the same fiber paths for all plies, as opposed to the solutions that explored the augmented design space, even with the inclusion of the manufacturing constraint. For illustration, the optimal fiber trajectories for configurations **O6** and **O7** are depicted in Fig. 11.

VII. Summary and conclusions

The theoretical modeling and numerical investigation on the aeroelastic-buckling stability optimization of tow-steered composite plates in the supersonic flow regime were presented in this paper.

The verified Rayleigh-Ritz based model was used to optimize tow-steered plates in a range of scenarios. Particular attention was devoted to constraints which must be imposed on fiber trajectories to avoid the occurrence of manufacturing defects, which must be dealt with in practical applications. Those constraints were considered by assuming fiber

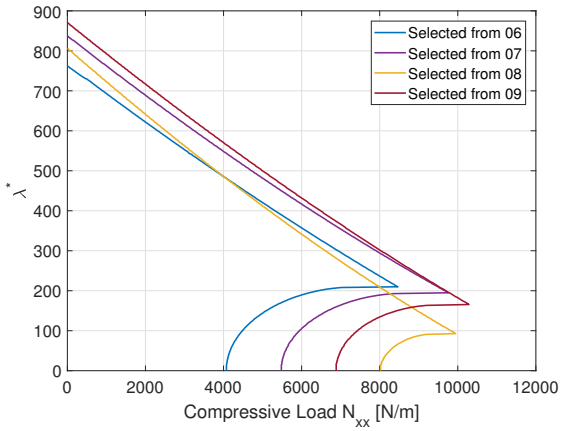

Fig. 10 **Combined flutter-buckling diagrams for selected configurations from O6, O7, O8 and O9.**

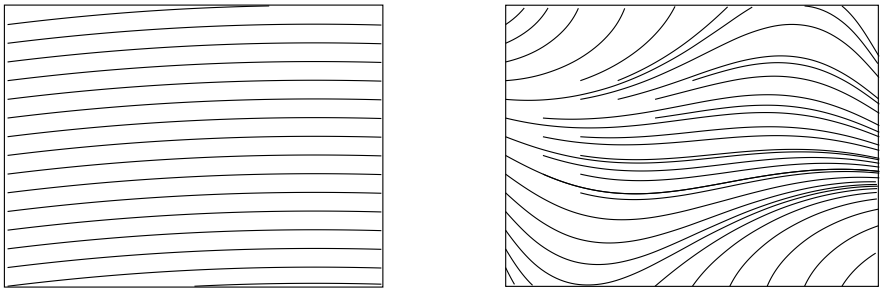

Fig. 11 **Optimized trajectories for selected configurations O6 and O7**

trajectories of constant radii, as suggested in the literature.

The numerical results obtained from optimization computations confirm previous findings that demonstrate that tow-steering is an effective means of improving both aeroelastic and buckling performance of composite plates as compared to traditional, unidirectional laminates. Additionally, it was observed that best performances are associated with plates having more complex fiber trajectories, which might not be feasible using current manufacturing capabilities.

It was observed that the consideration of manufacturing constraints such as enforcing fiber paths of constant radius in order to avoid manufacturing defects, considering the same path for all plies, could lead to virtually no improvements of flutter-buckling stability as compared to unidirectional laminates of same stacking sequence. Hence, an alternative strategy was considered (use of an augmented design space), which provided significant improvement of the stability margin and, even under manufacturing constraints.

It was also verified that constant turning radius constraint excessively reduces the design space and leads to unsatisfactory optimized configurations. Certainly, an intermediate and convenient scenario could be devised by constraining the minimum turning radius, without however enforcing constant curvature of the fiber paths. In this case, the modeling procedure should be adapted to include this constrain on the turning radius of the fiber paths using different

polynomial orders. In addition, tradeoffs between buckling/aeroelastic criteria and other design requirements, such as strength- and stiffness-related ones, can be searched in a multi-criteria optimization framework as the one suggested herein.

ACKNOWLEDGMENTS

The authors are thankful to Brazilian Research Agencies CNPq (Grants numbers 310633/2013-3 and 402238/2013-3), CAPES, FAPEMIG, FAPESP and the INCT-EIE for the continuous support to their research work.

References

[1] Dowell, E., "Nonlinear oscillations of a fluttering plate." *AIAA Journal*, Vol. 4, No. 7, 1966, pp. 1267–1275. doi:10.2514/3.3658, URL http://dx.doi.org/10.2514/3.3658.

[2] Dowell, E., "Panel flutter - A review of the aeroelastic stability of plates and shells," *AIAA Journal*, Vol. 8, No. 3, 1970, pp. 385–399. doi:10.2514/3.5680, URL http://dx.doi.org/10.2514/3.5680.

[3] Yang, T. Y., and SUNG, S. H., "Finite-element panel flutter in three-dimensional supersonic unsteady potential flow," *AIAA Journal*, Vol. 15, No. 12, 1977, pp. 1677–1683. doi:10.2514/3.7472, URL http://arc.aiaa.org/doi/abs/10.2514/3.7472.

[4] Xue, D. Y., and MEI, C., "Finite element nonlinear panel flutter with arbitrary temperatures in supersonic flow," *AIAA Journal*, Vol. 31, No. 1, 1993, pp. 154–162. doi:10.2514/3.11332, URL http://dx.doi.org/10.2514/3.11332.

[5] Shore, C. P., MEI, C., and GRAY, C. E., "Finite element method for large-amplitude two-dimensional panel flutter at hypersonic speeds," *AIAA Journal*, Vol. 29, No. 2, 1991, pp. 290–298. doi:10.2514/3.10576, URL http://dx.doi.org/10.2514/3.10576.

[6] Zhou, R. C., Lai, Z., Xue, D. Y., Huang, J.-K., and Mei, C., "Suppression of nonlinear panel flutter with piezoelectric actuators using finite element method," *AIAA Journal*, Vol. 33, No. 6, 1995, pp. 1098–1105. doi:10.2514/3.12530, URL http://arc.aiaa.org/doi/abs/10.2514/3.12530.

[7] Castro, S. G. P., Guimarães, T. A. M., Rade, D. A., and Donadon, M. V., "Flutter of stiffened composite panels considering the stiffener's base as a structural element," *Composite Structures*, Vol. 140, 2016, pp. 36–43. doi:http://dx.doi.org/10.1016/j.compstruct.2015.12.056, URL http://www.sciencedirect.com/science/article/pii/S0263822315011460.

[8] Hasheminejad, S. M., and Aghayi Motaaleghi, M., "Aeroelastic analysis and active flutter suppression of an electro-rheological sandwich cylindrical panel under yawed supersonic flow," *Aerospace Science and Technology*, Vol. 42, 2015, pp. 118–127. doi:http://dx.doi.org/10.1016/j.ast.2015.01.004, URL http://www.sciencedirect.com/science/article/pii/S127096381500019X.

[9] Marques, F., Natarajan, S., and Ferreira, A., "Evolutionary-based aeroelastic tailoring of stiffened laminate composite panels in supersonic flow regime," *Composite Structures*, Vol. 167, 2017, pp. 30 – 37. doi:https://doi.org/10.1016/j.compstruct.2017.01.062, URL http://www.sciencedirect.com/science/article/pii/S0263822316326691.

[10] Shirk, M. H., Hertz, T. J., and Weisshaar, T. A., "Aeroelastic tailoring - Theory, practice, and promise," *Journal of Aircraft*, Vol. 23, No. 1, 1986, pp. 6–18. doi:10.2514/3.45260.

[11] Lopes, C., Gürdal, Z., and Camanho, P., "Variable-stiffness composite panels: Buckling and first-ply failure improvements over straight-fibre laminates," *Computers and Structures*, Vol. 86, No. 9, 2008, pp. 897 – 907. doi:http://dx.doi.org/10.1016/j.compstruc.2007.04.016, URL http://www.sciencedirect.com/science/article/pii/S0045794907001654, composites.

[12] Hyer, M. W., and Charette, R. F., "Use of curvilinear fiber format in composite structure design," *AIAA Journal*, Vol. 29, No. 6, 1991, pp. 1011–1015. doi:10.2514/3.10697, URL http://dx.doi.org/10.2514/3.10697.

[13] Akhavan, H., and Ribeiro, P., "Natural modes of vibration of variable stiffness composite laminates with curvilinear fibers," *Composite Structures*, Vol. 93, No. 11, 2011, pp. 3040 – 3047. doi:http://dx.doi.org/10.1016/j.compstruct.2011.04.027, URL http://www.sciencedirect.com/science/article/pii/S0263822311001516.

[14] Stodieck, O., Cooper, J. E., Weaver, P. M., and Kealy, P., "Improved aeroelastic tailoring using tow-steered composites," *Composite Structures*, Vol. 106, 2013, pp. 703–715. URL http://www.sciencedirect.com/science/article/pii/S0263822313003462.

[15] Stanford, B. K., Jutte, C. V., and Chauncey Wu, K., "Aeroelastic benefits of tow steering for composite plates," *Composite Structures*, Vol. 118, 2014, pp. 416–422. URL http://www.sciencedirect.com/science/article/pii/S0263822314003973.

[16] Stodieck, O., Cooper, J. E., Weaver, P. M., and Kealy, P., "Optimization of Tow-Steered Composite Wing Laminates for Aeroelastic Tailoring," *AIAA Journal*, Vol. 53, No. 8, 2015, pp. 2203–2215. doi:10.2514/1.J053599, URL https://doi.org/10.2514/1.J053599.

[17] Guimarães, T. A. M., "Contributions to study of Dynamic and Aeroelastic behaviour of Variable Stiffness Composite Laminates (in portuguese)," Ph.D. thesis, Federal University of Uberlândia - Scholl of Mechanic Engineering, 2016.

[18] Fazilati, J., "Panel flutter of curvilinear composite laminated plates in the presence of delamination," *Journal of Composite Materials*, 2018. doi:10.1177/0021998318754641.

[19] Akhavan, H., and Ribeiro, P., "Geometrically non-linear periodic forced vibrations of imperfect laminates with curved fibres by the shooting method," *Composites Part B: Engineering*, 2016. doi:http://dx.doi.org/10.1016/j.compositesb.2016.10.059, URL http://www.sciencedirect.com/science/article/pii/S1359836816311726.

[20] Fayazbakhsh, K., Arian Nik, M., Pasini, D., and Lessard, L., "Defect layer method to capture effect of gaps and overlaps in variable stiffness laminates made by Automated Fiber Placement," *Composite Structures*, Vol. 97, 2013, pp. 245–251. doi:http://dx.doi.org/10.1016/j.compstruct.2012.10.031, URL http://www.sciencedirect.com/science/article/pii/S0263822312005272.

[21] Akbarzadeh, A. H., Arian Nik, M., and Pasini, D., "Vibration responses and suppression of variable stiffness laminates with optimally steered fibers and magnetostrictive layers," *Composites Part B: Engineering*, Vol. 91, 2016, pp. 315–326. doi:http://dx.doi.org/10.1016/j.compositesb.2016.02.003, URL http://www.sciencedirect.com/science/article/pii/S1359836816001037.

[22] Wu, Z., Weaver, P. M., Raju, G., and Chul Kim, B., "Buckling analysis and optimisation of variable angle tow composite plates," *Thin-Walled Structures*, Vol. 60, 2012, pp. 163–172. doi:http://dx.doi.org/10.1016/j.tws.2012.07.008, URL http://www.sciencedirect.com/science/article/pii/S0263823112001930.

[23] Tsai, H., *Introduction to composite materials*, Lancaster: Technomic, 1980.

[24] Jones, R., *Mechanics of composite materials*, CRC, 1998.

[25] Craig, R., and Kurdila, A., *Fundamentals of Structural Dynamics*, Wiley, 2006.

[26] AIAA Education Series, American Institute of Aeronautics and Astronautics, 1999, Chap. Aeroelasticity Of Plates And Shells, pp. 229–289. doi:10.2514/5.9781600862458.0229.0289, 0.

[27] Guimaraes, T., Pereira, D. A., and Rade, D. A., "Dynamic Behavior and Optimization of Composite Tow Steered Plates," *Proceedings of the XVII International Symposium on Dynamic Problems of Mechanics*, edited by A. T. Fleury, D. A. Rade, and P. R. G. Kurka, ABCM, 2017.

[28] Guimaraes, T., Pereira, D. A., de Mello, W., and Rade, D. A., "Uncertainty Propagation and Optimization of the Dynamic Behavior of Tow Steered Composite Plates," *Proceedings of the International Conference on Structural Engineering Dynamics*, 2017.

[29] Manan, A., Vio, G. A., Harmin, M. Y., and Cooper, J. E., "Optimization of aeroelastic composite structures using evolutionary algorithms," *Engineering Optimization*, Vol. 42, No. 2, 2010, pp. 171–184. doi:10.1080/03052150903104358, URL https://doi.org/10.1080/03052150903104358.

[30] Lobato, F. S., and Steffen, V., Jr, "A new multi-objective optimization algorithm based on differential evolution and neighborhood exploring evolution strategy," *Journal of Artificial Intelligence and Soft Computing Research*, Vol. Vol. 1, No. 4, 2011, pp. 259–267.

[31] Falcó, O., Mayugo, J. A., Lopes, C. S., Gascons, N., Turon, A., and Costa, J., "Variable-stiffness composite panels: As-manufactured modeling and its influence on the failure behavior," *Composites Part B: Engineering*, Vol. 56, 2014, pp. 660–669. doi:http://dx.doi.org/10.1016/j.compositesb.2013.09.003, URL http://www.sciencedirect.com/science/article/pii/S1359836813005167.

[32] Waldhart, C., Gurdal, Z., and Ribbens, C., Structures, Structural Dynamics, and Materials and Co-located Conferences, American Institute of Aeronautics and Astronautics, 1996, Chaps. Analysis of tow placed, parallel fiber, variable stiffness laminates. doi:10.2514/6.1996-1569, URL https://doi.org/10.2514/6.1996-1569, 0.